Talanta 311 (2027) 130238

Contents lists available at ScienceDirect

Talanta

journal homepage: www.elsevier.com/locate/talanta

Resolution of chiral drug cocrystals: complementary roles of NMR, low-frequency Raman and vibrational circular dichroism

Věra Schrenková [a,b], Adam Sklenář [a,b], Martin Dračínský [a], Jan Rohlíček [c], Petr Bouř [a,b], Argyro Chatziadi [b], Jakub Kaminský [a,b,*]

[a] Institute of Organic Chemistry and Biochemistry, Academy of Sciences, Flemingovo nám. 2, Prague, 16610, Czech Republic
[b] University of Chemistry and Technology Prague, Technická 5, Prague, 16628, Czech Republic
[c] Institute of Physics, Academy of Sciences, Na Slovance 1999/2, Prague, 182 00, Czech Republic

ARTICLE INFO

Dataset link: Resolution Of Chiral Drug Cocrystals: Complementary Roles Of NMR, Terahertz Raman And Vibrational Circular Dichroism (Original data)

Keywords:
Cocrystals
Diastereomers
Vibrational circular dichroism
NMR
Raman spectroscopy

ABSTRACT

Reliable discrimination of diastereomeric pharmaceutical cocrystals remains a significant analytical challenge, particularly when structural differences are subtle or when monocrystals suitable for X-ray diffraction are not available or difficult to prepare. Here, we compare the performance of four spectroscopic techniques, solid-state nuclear magnetic resonance (ssNMR), Raman spectroscopy, infrared (IR) absorption, and solid-state vibrational circular dichroism (ssVCD), in terms of the resolution of model diastereomeric cocrystals. The first pair of diastereomeric cocrystals, (*S*)-naproxen with (*R*)- and (*S*)-alanine, represents an example of systems with pronounced packing differences, whereas the cocrystals of (*R*)-ivabradine hydrochloride with (*R*)- and (*S*)-mandelic acid are nearly isostructural diastereomers. The NMR and vibrational spectra were interpreted based on density functional theory (DFT) simulations, allowing for a detailed spectra-structure assignment and analysis. Although all techniques detected cocrystal formation, their practical discriminatory power toward diastereomers varied. VCD spectroscopy provided reliable differentiation, even for nearly isostructural systems, although the data were hampered by the experimental noise. Raman spectroscopy, especially in the low-frequency region, was effective for a rapid detection of distinct packing motifs but less sensitive for the closely related structures. ssNMR provides a complementary localized insight. The results indicate the advantages and drawbacks of using Raman spectroscopy, ssNMR, and VCD for screening, structural studies, and chiral identification of pharmaceutical cocrystals and other chiral complex solid-state systems.

1. Introduction

Active pharmaceutical ingredients (APIs), the main components of drugs, are preferentially administered orally in various solid-state formulations, such as polymorphs, amorphous forms, salts, hydrates, or solvates. Newly designed solid forms often improve the physicochemical properties important for therapeutic use [1–5]. These include solubility, bioavailability, mechanical resistance, easier manufacturing, pharmacokinetics, stability, or the taste [1,6–11]. Among the diverse solid forms, cocrystals have emerged as a particularly versatile strategy for tailoring the drug performance. They are typically composed of an API and a neutral coformer [12–14] and became standard in modern drug formulation, particularly after regulatory rules concerning cocrystals were amended by drug agencies, which made them easier to patent [14,15]. Cocrystals containing two different APIs are also being developed [16,17], e.g., for combination therapies [18]. Cocrystal preparation includes a plethora of methods, such as solvent-based crystallization, grinding, spray drying, or hot-melt extrusion [19].

Cocrystals are often characterized using X-ray diffraction, thermal analyses, spectroscopic and other techniques [20–25]. For example, solid-state nuclear magnetic resonance (ssNMR) can detect local conformation, hydrogen bonds and proton transfer [26–29], salt and cocrystal forms [30–35], stoichiometry [36], and trace anhydrous polymorph [37] or API [38]. Vibrational spectroscopy may often offer faster and cheaper analyses [7,39–42]. Raman spectra, particularly in the low-frequency (LF) region, carry information about intermolecular interactions and crystal packing [43–52]. Also, the surface-enhanced Raman scattering (SERS) extends the capabilities of conventional Raman spectroscopy by providing enhanced sensitivity toward molecules located close to a metal particle [53]. First SERS studies of crystal

* Corresponding author. Institute of Organic Chemistry and Biochemistry, Academy of Sciences, Flemingovo nám. 2, Prague, 16610, Czech Republic.
E-mail address: jakub.kaminsky@uochb.cas.cz (J. Kaminský).

https://doi.org/10.1016/j.talanta.2026.130238
Received 26 May 2026; Received in revised form 24 June 2026; Accepted 30 June 2026
Available online 3 July 2026
0039-9140/© 2026 The Authors. Published by Elsevier B.V. This is an open access article under the CC BY-NC license (http://creativecommons.org/licenses/by-nc/4.0/).

surfaces have been published demonstrating its usability in solid-state applications; however, the technique currently struggles with many challenges in terms of reproducibility, substrate preparation, quantitative interpretation, and solid-form stability [54]. Vibrational circular dichroism (VCD) is sensitive both to the structure and chirality [55,56], sensing crystal packing [55–57], polymorphs [57,58], and cocrystals [59–61].

More than half of marketed drugs are chiral [62] and diastereomeric salts or cocrystals are often developed to enable isolation of the desired enantiomer [62–64]. Typically, a diastereomeric cocrystal contains an enantiomerically pure compound A crystallized with both enantiomers of a compound B. Unlike enantiomers, which have identical physical properties, diastereomers may differ in crystal structure, solubility melting point, etc. [42,65]. In contrast to salts, where the formation of a diastereomeric pair of salts is the prevailing rule, cocrystal systems frequently exhibit enantiospecific behavior [66,67]. In pharmaceutical practice, cocrystallization using a single enantiomer of a coformer is typically exploited in enantiomeric resolution. In contrast, cocrystals of a single API configuration with different coformer enantiomers are being studied to elucidate the mechanisms governing the formation, stability, and selectivity of cocrystals [68]. Understanding of such mechanisms can make the cocrystals development more efficient [65].

Although spectroscopic detection of cocrystal or salt formation is relatively well-documented [69], spectroscopic differentiation of chiral diastereomers is rare [70]. It has been shown that diastereomeric cocrystals with substantially different intermolecular interaction patterns and/or different crystal packing can be distinguished by ssNMR [65,70,71]. Infrared (IR) spectroscopy was also able to distinguish between selected diastereomers, although the differences were not profound [59,70,72]. In LF Raman experiments, chiral components were occasionally investigated as well [10,52,73–75]. Still, a systematic understanding of how different techniques perform in discriminating diastereomeric cocrystals is lacking. The sensitivity of these methods to varying structures has not yet been comprehensively evaluated, which limits the use of many techniques for cocrystal development and control.

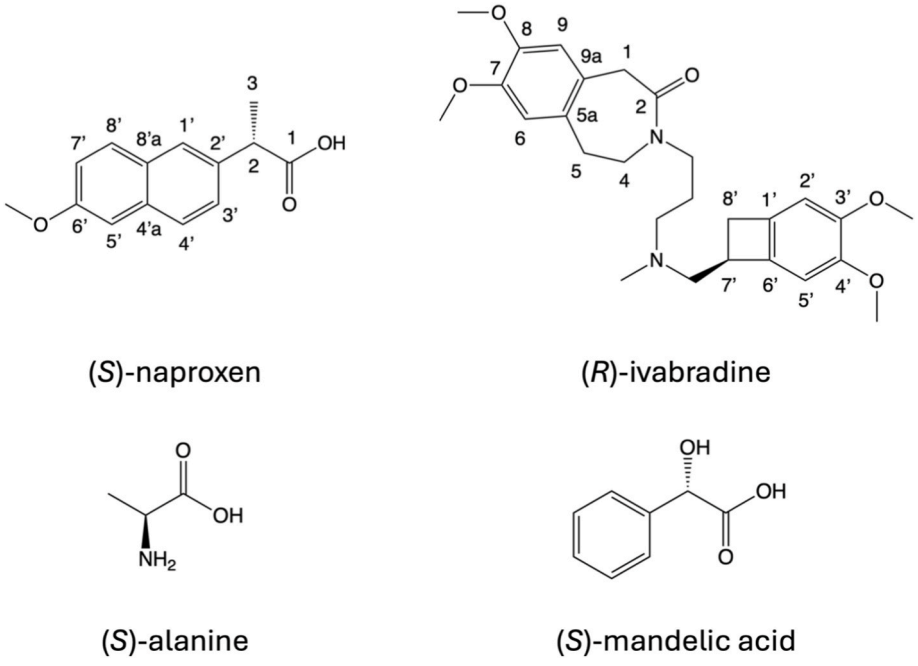
In this study, we address this challenge by comparing ssNMR, low-frequency Raman, IR, and VCD spectroscopies applied to two model pharmaceutical systems representing distinct structural regimes. Cocrystals of (*S*)-naproxen with (*R*)- and (*S*)-alanine represent structurally very distinct diastereomers [76], while cocrystals of (*R*)-ivabradine hydrochloride with (*R*)- and (*S*)-mandelic acid exhibit only subtle variations in the structure [9]. Naproxen is an anti-inflammatory drug commonly cocrystallizing with various compounds [13,76,77]. Ivabradine hydrochloride is a pharmaceutical salt used to treat chronic angina pectoris and chronic heart failure [78] existing in various polymorphic forms, solvates and salts [9] with good stability [9]. Experimental results are supported by density functional theory (DFT) calculations, enabling better spectral assignments and interpretation. We believe that the results may be helpful when applying these spectroscopic methods to chiral crystalline compounds and elucidating the structural origins of the observed spectral patterns.

2. Methods

2.1. Sample preparation

Enantiomers of alanine and mandelic acid, (*S*)-naproxen (Scheme 1), and potassium bromide were purchased from Sigma-Aldrich (≥97%). (*R*)-Ivabradine hydrochloride (Scheme 1) was kindly provided by Zentiva. Following previously published procedure [59,76], (*S*)-naproxen/(*R*)-alanine and (*S*)-naproxen/(*S*)-alanine were crystallized by the liquid-assisted grinding following Latif et al. [79] Naproxen and alanine were ground under ambient conditions at a frequency of 30 Hz for 60 min in a 1:1 stoichiometric ratio (100:39 mg) with a small quantity of methanol (10 µl per 100 mg of the mixture). A Retsch mixer mill MM 200 with three stainless-steel balls with a diameter of 0.5 cm was used for milling.

The (*R*)-ivabradine hydrochloride/(*R*)-mandelic acid and (*R*)-ivabradine hydrochloride/(*S*)-mandelic acid co-crystals were prepared according to conditions reported previously [9]. The (*R*)-ivabradine hydrochloride/(*R*)-mandelic acid cocrystal was prepared by liquid-assisted grinding of 100 mg of the API and coformer in an equimolar ratio using mortar and pestle for 10 min with 20 µL of acetone. The (*R*)-ivabradine hydrochloride/(*S*)-mandelic acid cocrystal was prepared analogously by liquid-assisted grinding for 10 min with 20 µL of ethyl acetate. All crystal structures were confirmed and characterized by PXRD, as in Ref. [9] and Ref. [59], and by their ssNMR and IR spectra matching published data [9,59,79].



Scheme 1. Studied APIs (top) with carbon atom numbering indicated and (*S*)-enantiomers of the coformers used (bottom).

2.2. NMR measurement

High-resolution ^{13}C ssNMR spectra were acquired on a JEOL ECZ600R spectrometer operating at 600.2 MHz for ^{1}H and 150.9 MHz for ^{13}C nuclei. The samples were loaded into 3.2-mm magic angle spinning rotors, and measurements were conducted at 18 kHz. Cross-polarization with a ramped amplitude shape pulse was employed to acquire the ^{13}C spectra. The contact time was set to 5 ms. To determine the relaxation delays, the proton T_1 relaxation times were estimated from the ^{1}H saturation recovery experiments. The relaxation delay was set to 1.5 times the corresponding T_1 time. All chemical shifts were referenced against the downfield CH signal of external adamantane ($\delta(^{13}C) = 38.5$ ppm).

2.3. Pellet preparation for Raman and VCD experiments

The cocrystals and KBr (Sigma-Aldrich, ≥97%) were finely ground together in an agate mortar in approximately 1:1 (Raman) and 1:100 M ratios (VCD). In the VCD experiment, the final ratio was adjusted to maintain the absorbance within 0.8–1.0, to prevent detector saturation and acceptable signal to noise ratio. The mixtures were compressed into thin transparent pellets of 7 mm diameter using a Specac Mini Pellet Press.

2.4. Raman spectroscopy

Raman experiments were performed using WITec Alpha 300RS confocal Raman microscope. Raman mapping of the pellets was performed in the backscattering geometry, using 10× dry objective (Zeiss EC Epiplan, numerical aperture 0.25). A laser wavelength of 532 nm with a power of 19 mW and an 1800 g/mm diffraction grating for spectra below 200 cm^{-1} or 600 g/mm grating for spectra up to 3500 cm^{-1} were used. The 532 nm excitation provides relatively efficient Raman scattering (even in the LF region) with low signal-to-noise ratio while avoiding resonance effects for the investigated pharmaceutical cocrystals. The mapping was performed with 2 μm steps and 1 s integration time for an area of 300 × 300 μm (150×150 points). Thus, each image consisted of 22 500 spectra. Raman maps were then pre-processed using WITec Project 5.1 software. First, we used a cosmic ray removal filter (filter size 4, dynamic factor 5), and the signal was averaged over all pixels for each compound. Baseline was subtracted from the spectra using our own implementation of the rubber band algorithm [80]. Additional details on the Raman experiment are in the Supplementary material.

2.5. VCD measurement

VCD and IR absorption spectra were recorded on a ChiralIR-2X™ spectrometer (BioTools, Inc., USA) equipped with a dual-PEM™ system using two ZnSe photoelastic modulators, following a previously established procedure [57]: 4 cm^{-1} resolution, the Blackman-Harris apodization function, and PEM calibration at 1400 cm^{-1}. The resulting spectra are the averages of six recorded blocks, each consisting of 1560 scans, and their accumulation lasted 3 h for each sample. The samples were rotated around the beam axis during spectrum recording. The baseline was subtracted using the spectra of the KBr matrix measured using the same parameters.

2.6. Simulations of NMR spectra

NMR shieldings were computed using the CASTEP program, version 22.11 [81], employing density functional theory (DFT), pseudopotentials to model core electron effects, and plane waves to describe valence electrons. Before conducting the NMR calculations, the atomic positions of all atoms were optimized while maintaining fixed unit cell parameters. The geometry optimization was conducted utilizing the GGA Perdew–Burke–Ernzerhof (PBE) functional [82], plane wave basis set energy cutoff at 600 eV, default ultrasoft [83] "on-the-fly-generated" pseudopotentials, and a minimum k-point spacing of 0.1 $Å^{-1}$ over the Brillouin zone via the Monkhorst–Pack grid [84]. Empirical dispersion corrections using the TS correction scheme was used [85]. The GIPAW approach was used for NMR calculations under periodic conditions at the same computational level as that for geometry optimizations [86, 87].

2.7. Simulations of vibrational spectra

The initial geometries of the cocrystals were imported from the X-ray crystallographic database [88] (CCDC entries: 985631 [76], 985632 [76], 1479091 [9], or 1479092 [9]) using the Mercury program [89].

Three strategies were used to refine the positions of the hydrogen atoms. In the first approach (OPT1), the geometry of the unit cell was optimized in the CASTEP program using the OTFG norm-conserving pseudopotentials, 990 eV energy cut-off, ultra-fine SCF criteria, the PBE functional [82] with the G06 dispersion correction [90]. and a Brillouin zone fine k-point setup of 1 × 2 × 1. The lattice size was fixed. In the second (OPT2), a larger crystal fragment consisting of 3 × 3 × 3 unit cells was built, and pairs of close molecules were detected and partially optimized in the normal mode coordinates [91], using the QGRAD code [92] linked to Gaussian 16 [93], at the B3LYP/6-311++G (d,p) level of theory. The environment of a crystal bulk was mimicked using the CPCM model [94] with parameters for water, which appeared as a viable approximation previously [39,49,57]. Normal mode coordinates of frequencies greater than 100 cm^{-1} were relaxed. In the third approach (OPT3), the crystal unit cell was optimized using CASTEP for the crystal and normal mode optimization of the pairs.

For the pairs, the harmonic force field, polarizability derivatives (for Raman), and atomic polar and axial tensors (for IR and VCD) were calculated using the Gaussian program [93] at the B3LYP/6-311++G(d, p)/CPCM level of theory. The atomic property tensors were transferred back to the 3 × 3 × 3 crystal fragment using the Cartesian coordinate transfer implemented in the *cctn* program [95], which allowed us to construct a dynamic force field matrix involving interactions within the elementary cell and its close environment. Finally, the harmonic vibrational frequencies, IR, VCD, and Raman intensities were calculated for the zero (0, 0, 0) crystal phonon mode. The line intensities were convoluted with Lorentzian bands of 10 cm^{-1} full width at half-height. No scaling factor was used in the calculations to correct the DFT frequencies.

To compare predicted spectra with experimental ones, spectral similarity indices were calculated as $\sigma = \int \frac{S_{exp,1} S_{exp,2} d\upsilon}{\left(\int S^2_{exp,1} d\upsilon \int S^2_{exp,2} d\upsilon\right)^{1/2}}$. Integrals were calculated over the 20−200 cm^{-1} region for LF Raman spectra, 200-1800 cm^{-1} for fingerprint Raman spectra, and 800−1800 cm^{-1} for IR and VCD spectra.

3. Results and discussion

3.1. Cocrystals of naproxen and alanine

3.1.1. Structure and experimental spectra

The first diastereomeric pair studied was a cocrystal of (*S*)-naproxen with (*S*)- or (*R*)-alanine in a 1:1 ratio. The crystal packing of both cocrystals is compared in Fig. 1. In both cocrystals, (*S*)-naproxen is neutral, whereas alanine is zwitterionic. Alanine molecules are oriented "head-to-tail" interacting via charge-assisted hydrogen bonds and form infinite chains in the *ac* plane. This is a typical motif also for other crystalline amino acids [76]. These alanine chains form sandwich layers in the *b* axis stabilized by interactions between adjacent planes. The alanine molecules are further H-bonded to naproxen, whereas the naproxen molecules do not form H-bonds with one another. In the two diastereomeric cocrystals, the intermolecular H-bonding distances are similar,

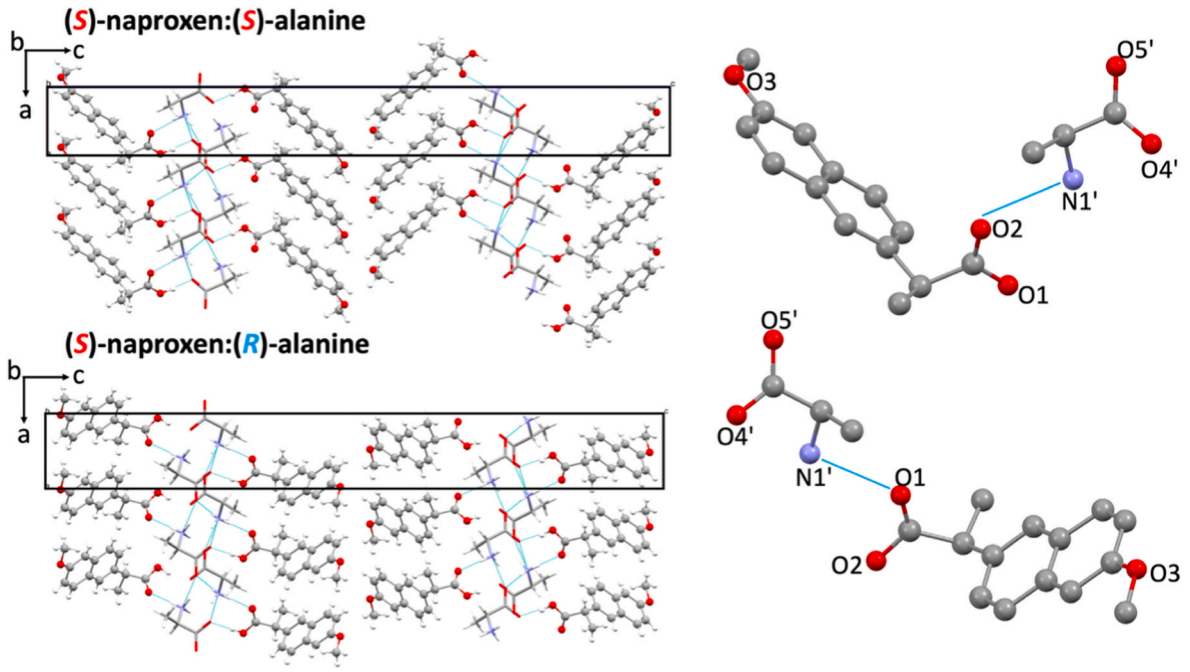


Fig. 1. X-ray structures of (*S*)-naproxen/(*S*)-alanine (top) and (*S*)-naproxen/(*R*)-alanine (bottom) cocrystals. H-bonds are indicated by blue lines. The H-bonded parts are magnified on the right.

which was also well reproduced by calculations (Table S1).

For the (*S*)-naproxen/(*S*)-alanine cocrystal, the structure allows π-π interactions among naproxen molecules, while for the (*S*)-naproxen/(*R*)-alanine cocrystal, a higher proportion of CH-π interactions was observed [76]. PXRD confirmed that our prepared cocrystals correspond to previously published structures (Fig. S1) [79].

The solid-state ^{13}C NMR spectra of (*S*)-naproxen/(*S*)-alanine and (*S*)-naproxen/(*R*)-alanine cocrystals without the silent region are shown in Fig. 2. The complete spectra are shown in Fig. S2. Moderate but clearly visible differences were observed between the two cocrystals. The signal assignment was performed by comparison with solution-state ^{13}C spectra and DFT calculations (see section 3.1.2). The largest differences between the cocrystals can be observed for the signal of carbon atom at positions C4 (128.1 ppm in (*S*)-naproxen/(*R*)-alanine, 125.0 in (*S*)-naproxen/(*S*)-alanine), C8 (130.7 or 132.9 in (*S*)-naproxen/(*R*)-alanine, 128.0 in (*S*)-naproxen/(*S*)-alanine), C1 (123.4 in (*S*)-naproxen/(*R*)-alanine, 121.5 in (*S*)-naproxen/(*S*)-alanine), C3 (128.1 in (*S*)-naproxen/(*R*)-alanine, 126.2 in (*S*)-naproxen/(*S*)-alanine), and at C2′ 43.6 in (*S*)-naproxen/(*R*)-alanine, 42.0 in (*S*)-naproxen/(*S*)-alanine).

For control, we inspected the Raman spectrum of a 1:1 mixture, which was within the experimental error indistinguishable from the arithmetic average of the individual component spectra, including the LF region (Fig. S3). This indicates that milling did not alter the microscopic structure or spectral response. Raman spectra of the (*S*)-naproxen/alanine cocrystals differ from such plain sum (Fig. 3), confirming their applicability for monitoring the formation of cocrystals. For example, the band of naproxen at 1728 cm^{-1} (C═O1 and O–H stretching, see Table S2 for the assignment) decreases in intensity, and

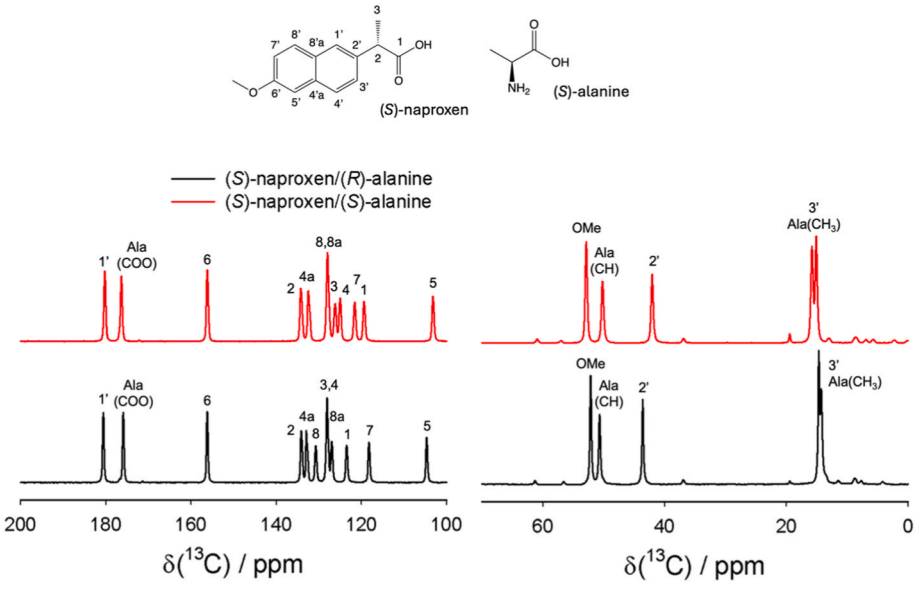


Fig. 2. Experimental ^{13}C NMR spectra of cocrystals of (*S*)-naproxen with (*R*)-and (*S*)-alanine (Region 100–70 ppm without signal is omitted.).

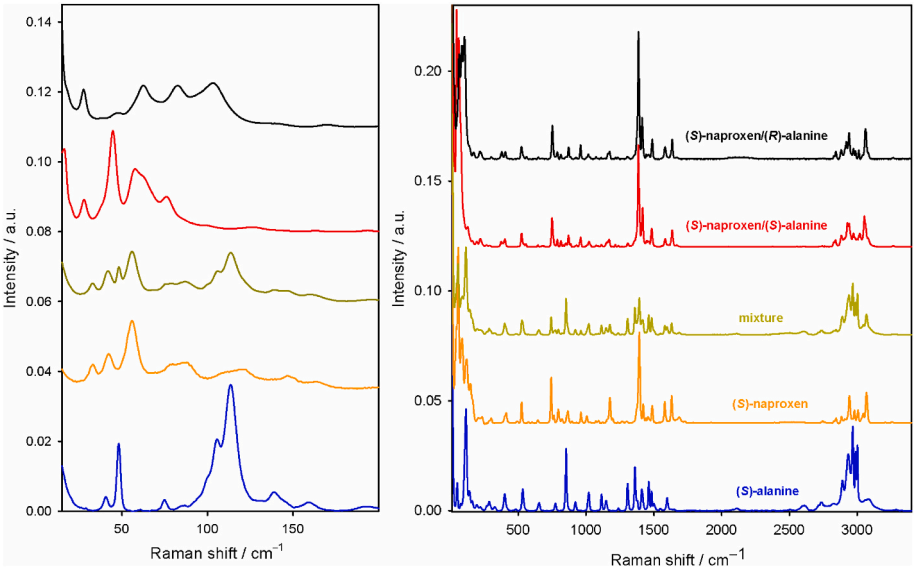


Fig. 3. Experimental Raman spectra of cocrystals of (*S*)-naproxen with (*R*)- and (*S*)-alanine, their mixture in a 1:1 M ratio, (*S*)-naproxen, (*R*)-alanine, and (*S*)-alanine. The low-wavenumber region is magnified on the left. The spectra of (*S*)-naproxen, the mixture, and cocrystals were offset from (*S*)-alanine by 0.04, 0.06, 0.08, and 0.11 a.u. (LF-region) and by 0.04, 0.08, 0.12, and 0.16 a.u. (entire region).

the 1649 cm^{-1} NH_3^+ deformation band of alanine shifts to 1635 cm^{-1} due to the different H-bonding in the cocrystal. Similarly, upon cocrystallization, the 1598 cm^{-1} alanine band of the NH_3^+ deformation and valence C═O stretching shifted to 1585 cm^{-1}. The NH_3 deformation vibration becomes more pronounced and shifts from 1649 cm^{-1} to 1635 cm^{-1}, while the NH_3 deformation bands at 1361 cm^{-1} and 1307 cm^{-1} disappear. This indicates that the amino group plays a significant role in hydrogen bonding interactions.

The figure also shows that Raman spectroscopy is efficient in distinguishing individual diastereomers. In the LF region, the (*S*)-naproxen/(*S*)-alanine cocrystal exhibits intense bands at 28, 45, 56, and 78 cm^{-1}, whereas the (*S*)-naproxen/(*R*)-alanine cocrystal exhibits bands at 28, 63, 83, and 103 cm^{-1}, and the relative intensities are different as well. However, only modest differences are apparent in the fingerprint region above 200 cm^{-1}. These mostly involve minor frequency shifts, some of which are summarized in Table S2 (Supporting Information).

VCD and IR spectra of the (*S*)-naproxen/alanine cocrystals and their components are shown in Fig. 4, and the selected band frequencies and assignments are listed in Table S3. As with ssNMR and Raman spectroscopy, the formation of both cocrystals is clearly reflected in the IR and VCD spectra. For example, the C═O stretching band of naproxen (1728 cm^{-1}) and the analogous alanine band at 1597 cm^{-1} merged into a signal at 1667 cm^{-1} for both cocrystals. The +/− couplet of the NH_3 symmetric bending vibration in (*S*)-alanine shifts from 1620 cm^{-1} to

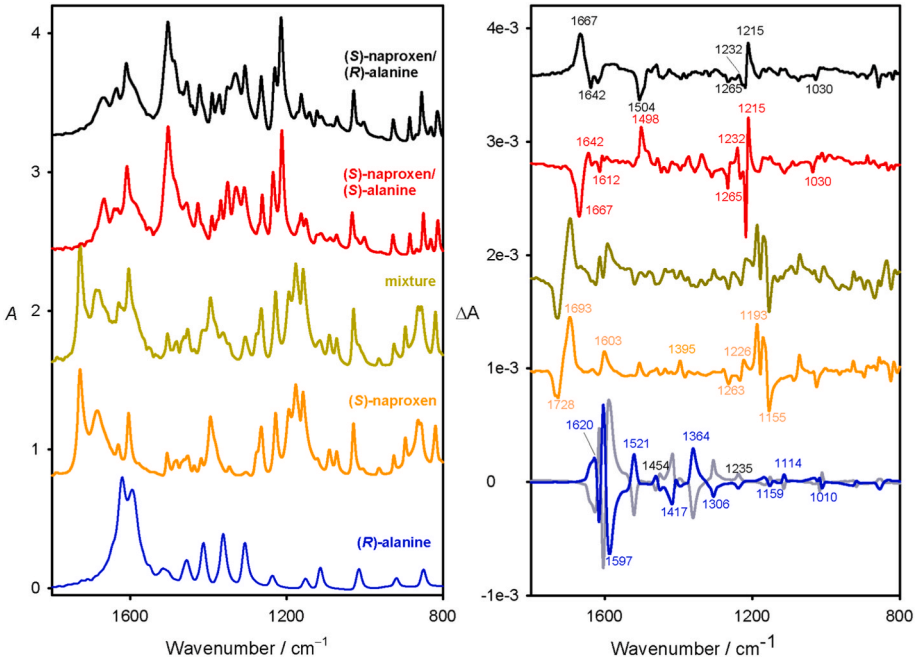


Fig. 4. Experimental VCD and IR spectra of cocrystals of (*S*)-naproxen with (*R*)- and (*S*)-alanine, their mixture in a 1:1 M ratio, (*S*)-naproxen, (*R*)-alanine, and (*S*)-alanine. The spectra of (*S*)-naproxen, the mixture, and cocrystals were offset from alanine by 0.8, 1.6, 2.4, and 3.2 (IR) and by 0.0009, 0.0018, 0.0027, and 0.0036 (VCD).

1612 cm^{-1} and sign-flips for (*S*)-naproxen/(*S*)-alanine. The alanine CH_3 bending band shifts from 1521 cm^{-1} to lower frequencies after cocrystallization (1504 and 1498 cm^{-1} for *SR* and *SS* cocrystals, respectively). As with Raman spectroscopy, there is no significant difference between VCD of the control mixture of cocrystal components in a 1:1 ratio and the average spectrum of these components (Fig. S3).

While the IR spectra of the two diastereomeric pairs exhibit only subtle differences (~1350 cm^{-1}; Fig. S4), the VCD spectra allow for clearer differentiation. The most useful VCD bands include the aforementioned C═O stretching and CH_3 bending of alanine. The carbonyl stretching band at 1667 cm^{-1} is negative for (*S*)-naproxen/(*S*)-alanine, and positive for (*S*)-naproxen/(*R*)-alanine. The CH_3 band is positive for (*S*)-naproxen/(*S*)-alanine but negative for (*S*)-naproxen/(*R*)-alanine. Unlike IR or Raman spectroscopy, VCD allows for the differentiation between enantiomers; that is, the absolute configuration can be assigned using this technique.

3.1.2. Computed NMR spectra of the naproxen cocrystals

The simulations help in better understanding and potentially guiding experimental observations. Fig. S5 shows the calculated ^{13}C NMR spectra of both naproxen cocrystals and the experiment. We observe overall good agreement, mostly within a few ppm difference of calculated and experimental shifts. The most pronounced deviation in the calculations can be observed for the two methyl signals at ~15 ppm, which was previously attributed to nuclear quantum effects in methyl groups [96].

3.1.3. Computed vibrational spectra of naproxen cocrystals

Simulated Raman, VCD and IR spectra somewhat differ for the three optimization procedures used (Fig. S6–S7, Table S4–S5). The combined method (OPT3) on average provided the best spectra if compared to the experiment, with similarity indices σ: 0.914, 0.761 and 0.746 for fingerprint Raman, LF Raman and IR spectra of (*S*)-naproxen/(*S*)-alanine; 0.901, 0.517 and 0.722 for fingerprint Raman, LF Raman and IR spectra of (*S*)-naproxen/(*R*)-alanine). The different optimization strategies mostly affect the LF Raman and IR bands around ~1215, ~1500 cm^{-1}, or the $\delta(NH_3^+)_{ala}$ and $\nu(C{=}O)_{nap}$ bands at ~1600 cm^{-1}.

Fig. S8 shows the VCD, IR, and Raman spectra simulated using the OPT3 approach, together with the experimental spectra. One can see that only some experimental VCD features were correctly reproduced by the calculation, which is primarily due to the approximations adopted because of limited computational power, as discussed in Ref. [49]. However, the main differences between the two cocrystal types are reproduced, such as the richer spectrum of (*S*)-naproxen/(*S*)-alanine compared to that of (*S*)-naproxen/(*R*)-alanine. For IR and Raman spectroscopy, the computations excellently capture the main differences between the two diastereoisomeric cocrystals.

3.2. Cocrystals of ivabradine hydrochloride and mandelic acid

3.2.1. Experimental data

Unlike naproxen/alanine, ivabradine/mandelic cocrystals are more complex because they consist of a salt (a two-component system) that further cocrystalizes with a coformer. The structures of the *RR* and *RS* ivabradine/mandelic acid cocrystals are compared in Fig. 5. Ivabradine is protonated at the acyclic amine nitrogen. Both diastereomers crystallize in the orthorhombic system ($P2_12_12_1$ space group) and exhibited similar crystal packing. They differ in the H-bonds caused by the different orientations of the hydroxyl group of mandelic acid. In the *RR* cocrystal, (*R*)-mandelic acid forms H-bonds with the chloride anion via its carboxyl group (O3–H···Cl^-) and with ivabradine carbonyl via its hydroxyl group (O1′–H···O2). The ivabradine nitrogen forms an H-bond with chlorine (N1′–H···Cl^-). In the *RS* cocrystal, (*S*)-mandelic acid forms H-bonds between O3–H···Cl^-, O2–H···Cl^-, and a weaker N1′–H···Cl^- [9]. The X-ray analysis also indicates somewhat shorter H-bonds in the (*R*)-ivabradine/(*R*)-mandelic acid cocrystal (Table S1). These structural differences are reflected in the higher melting point and density of the *RS* cocrystal compared to that of *RR*. PXRD confirmed that our prepared cocrystals correspond to previously published structures (Fig. S1) [9].

The main signals in the experimental ^{13}C NMR spectra of the two cocrystals are shown in Fig. 6 (cf. Fig. S9 shows the entire range). As in the case of naproxen/alanine, small differences in peak positions are apparent. The largest difference can be observed for the CH_2 group adjacent to the lactam ring (44.3 ppm in the (*R*)-ivabradine/(*R*)-mandelic acid cocrystal, 41.7 ppm in the (*R*)-ivabradine/(*S*)-mandelic acid cocrystal; labeled as lac-**C**H_2-) and the aliphatic C–H carbon of mandelic acid (73.3. ppm in *RR* and 71.0 ppm in *RS*; Mand.(C–OH)) and C7' (38.3 ppm in *RR* and 40.0 ppm in *RS*).

Raman spectra of (*R*)-ivabradine.HCl/(*S*)-mandelic acid and (*R*)-ivabradine.HCl/(*R*)-mandelic acid cocrystals are plotted in Fig. 7, assignment of some Raman bands is given in Table S6, comparison of calculated and experimental Raman bands is given in Table S7. Ivabradine exhibits much weaker Raman scattering than mandelic acid, so that the latter dominates in the 1:1 mixture. Upon cocrystallization, the Raman signal of ivabradine becomes more pronounced, in line with Ref. [9].

The differences between the *RR* and *RS* combinations are subtler than those for the naproxen/alanine system (compare the black and red spectra in Fig. 7). Unlike naproxen/alanine, the two forms can be more easily resolved in the fingerprint region. Minor changes in the positions

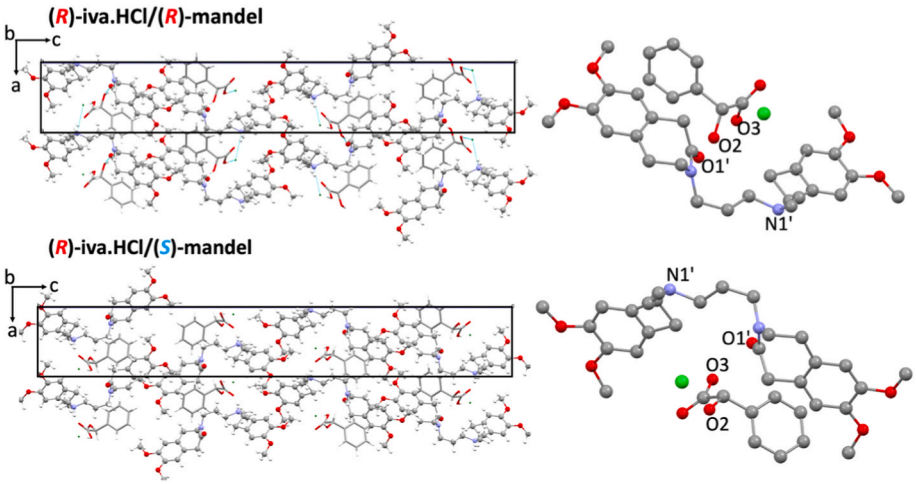


Fig. 5. Structures of the *RR* and *RS* ivabradine.HCl/mandelic acid cocrystals, and details of the H-bonded atoms.

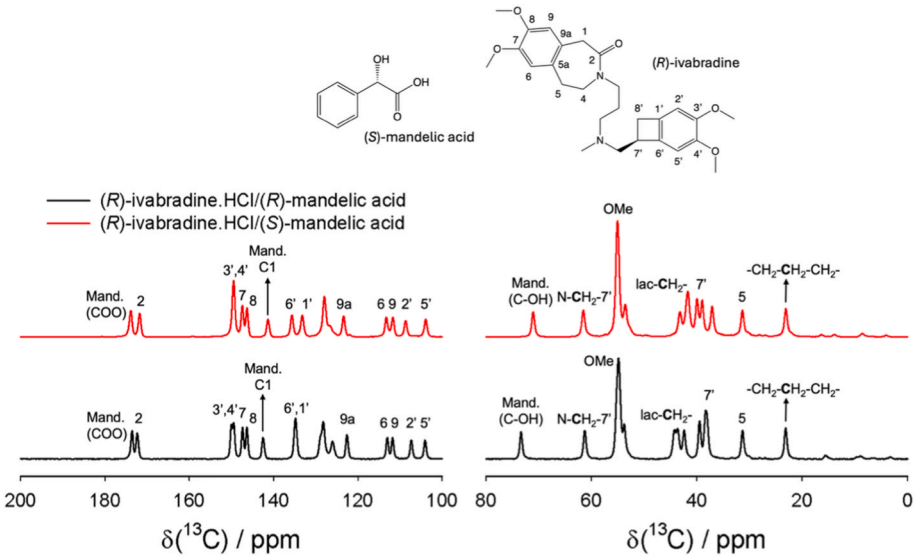


Fig. 6. Experimental ^{13}C NMR spectra of (*R*)-ivabradine hydrochloride/(*R*)-mandelic acid and (*R*)-ivabradine hydrochloride/(*S*)-mandelic acid cocrystals. Region 100-80 ppm without a signal is omitted.

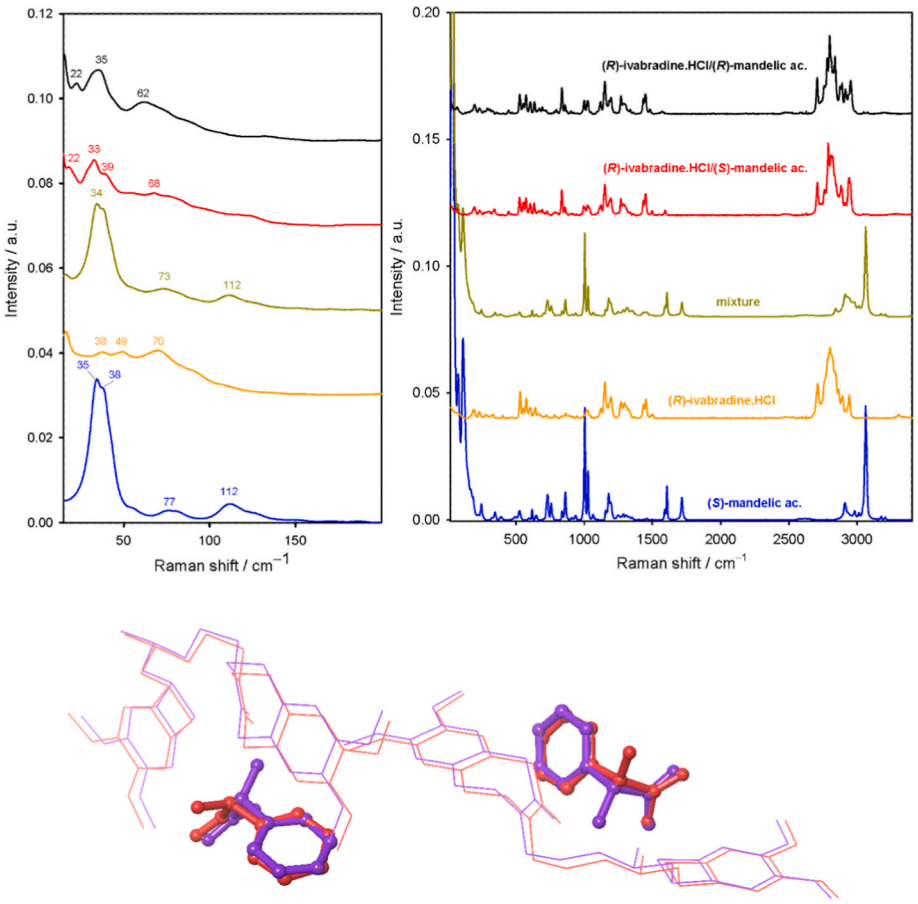


Fig. 7. Raman spectra (top) of (*R*)-ivabradine.HCl/(*R*)-mandelic acid and (*R*)-ivabradine.HCl/(*S*)-mandelic acid cocrystals, spectra of pure coformers and API, and their mixture in 1:1 M ratio. The spectra of (*R*)-ivabradine.HCl, the mixture, and cocrystals were offset from (*S*)-mandelic acid by 0.03, 0.05, 0.07, and 0.09 a.u. (LF-region) and by 0.04, 0.08, 0.12, and 0.16 a.u. (entire region). The overlay of the *RR* and *RS* structural fragments is at the bottom.

and shapes of bands above 1600 cm^{-1} and around 3000 cm^{-1} were already observed in the work of Sládková et al. [9] using a 1064 nm laser. Using the 532 nm laser, we also observe a difference in the position of the ν(C=O)$_{iva.HCl}$ band, which is at 1638 cm^{-1} for the (*R*)-ivabradine.HCl/(*R*)-mandelic acid cocrystal, while at ~1653 cm^{-1} for the other one. The similarity in the LF range is due to the similar packing of both diastereomers, with only slight differences in the mutual interactions of the molecules (Fig. 7, bottom). From the figure, it is

evident that the positions and conformations of ivabradines in both cocrystals are identical. Similarly, the positions of the aromatic rings and carboxyl groups of the mandelic acids are identical, and only the orientation of the hydroxyl groups differs.

IR and VCD spectra of both cocrystals and their components are shown in Fig. 8, and the band assignments are provided in Table S8. Clearly, VCD is more sensitive to structural changes than IR spectroscopy or NMR. In both the *RR* and *RS* cocrystals, the 1720 and 1744 cm^{-1} C=O bands of mandelic acid are both negative, whereas pure *S* and *R* mandelic acids give opposite signs at 1712 cm^{-1}. C=O bands of (*R*)-ivabradine (1661 and 1648 cm^{-1}) become weaker and shift to lower wavenumbers in the cocrystals. VCD bands at 1184 cm^{-1} and 1159 cm^{-1} (C–H vibrations near the quaternary nitrogen) are affected by the interaction between ivabradine hydrochloride and mandelic acid.

VCD also clearly distinguishes the cocrystals and the 1:1 ground mixture of (*R*)-ivabradine·HCl and (*S*)-mandelic acid. For example, the C=O stretching band shifts from 1723 cm^{-1} in the cocrystal to 1744 cm^{-1} in the mixture. This suggests that VCD can also detect minor differences in the carbonyl moiety. In contrast, LF Raman spectroscopy was unable to detect this subtle difference. The biggest differences between the VCD spectra of the ivabradine cocrystals appear in the carbonyl stretching regions of both ivabradine and mandelic acid. The negative $\nu(C{=}O)_{man}$ band at ~1744 cm^{-1} in the *RR* cocrystal shifts to ~1720 cm^{-1} in *RS*. Similarly, the $\nu(C{=}O)_{iva}$ band shifts from 1652 cm^{-1} to 1638 cm^{-1}. The intensity of the $\nu(C{=}O)_{man}$ band is also substantially higher for *RS* than for its diastereomer. However, in contrast to naproxen, the differences between the diastereomers are reflected only in the positions and intensities of the ν(C=O) bands, and not in their signs (Fig. S10). As with naproxen, there is no significant difference between Raman or VCD of the mixture of cocrystal components and plain sum of pure components (Fig. S11).

Interestingly, the VCD-to-IR signal ratios are very small for the cocrystals, approximately one order of magnitude smaller than those for the naproxen/alanine cocrystals. This may be related to weaker intermolecular interactions in ivabradine cocrystals compared to naproxen cocrystals, and long-range VCD contributions [97,98]. In addition, a large part of the system is composed of aromatic, intrinsically non-chiral residues.

3.2.2. *Computed NMR spectra of ivabradine cocrystals*

The simulated ^{13}C NMR spectra are compared with the experimental results in Fig. S12. Although the agreement between the calculations and the experiment is somewhat poorer than in the case of the naproxene cocrystals, it is still good, with most chemical shifts reproduced within a few ppm. Thus, although the differences between the (*R*)-ivabradine/(*R*)-mandelic acid and (*R*)-ivabradine/(*S*)-mandelic acid cocrystals are rather minor, the calculations reproduce the observed trends well. As with naproxen, the methyl signals at ~55 ppm remain problematic. In addition, the nearly overlapping experimental signals for C2 of ivabradine (~172 ppm) and mandelic acid carboxyl (~173 ppm) are unrealistically distinguished in the calculation. Remaining discrepancies do not affect the overall spectral assignment or the discrimination of the diastereomers based on lac-CH_2-, C7′ or Mand. (C–OH) (Fig. S13).

3.2.3. *Computed vibrational spectra of ivabradine cocrystals*

As with the naproxen cocrystals, the simulated Raman, VCD, and IR spectra somewhat differ for the three optimization procedures used (Fig. S14–S15), and the best OPT3 approach is used as the default in Fig. S16, where the simulations are compared to the experiments. A relatively good agreement was achieved for both diastereomers, with similarity indices σ: 0.867, 0.959 and 0.864 for fingerprint Raman, LF Raman and IR spectra of the *RR* diastereomer; 0.883, 0.966 and 0.858 for fingerprint Raman, LF Raman and IR spectra of the *RS* diastereomer. This is sufficient for phase identification, although detailed inconsistencies exist as well, similar to those observed with naproxen.

The adopted computational procedures were limited by the size of the crystal unit cell. For ivabradine/mandelic acid cocrystals it contains four molecules of ivabradine and four molecules of mandelic acid. The total of 364 atoms makes it too large for a direct simulation of Raman spectra using “periodic” codes like CASTEP. Moreover, the VCD calculations are not generally implemented in such programs, and the family

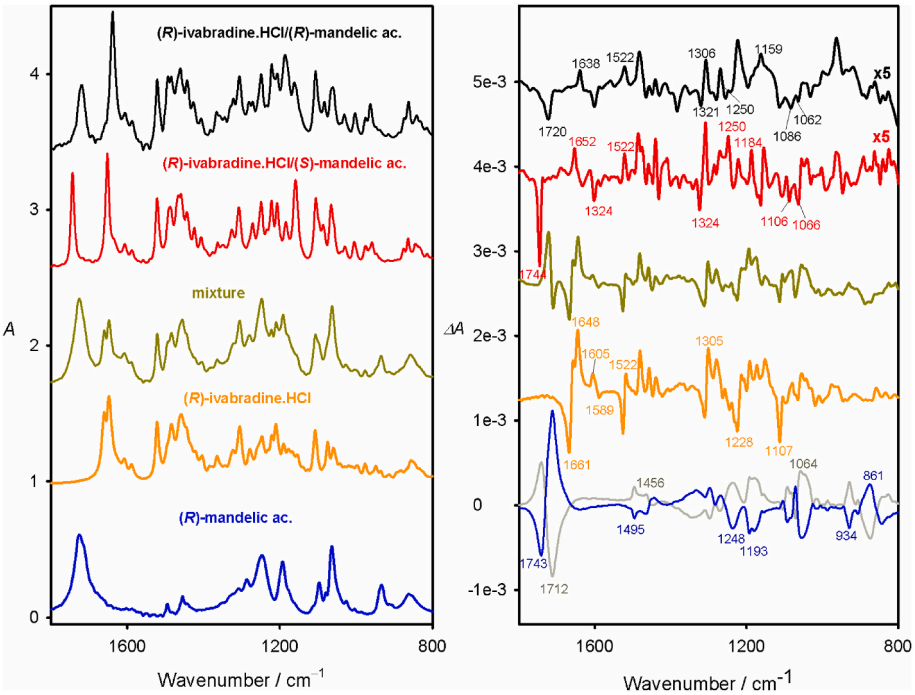


Fig. 8. Experimental IR and VCD spectra of (*R*)-ivabradine.HCl/(*R*)-mandelic acid (*R*)-ivabradine.HCl/(*S*)-mandelic acid cocrystals, their mixture in 1:1 M ratio, (*R*)-ivabradine, (*R*)-mandelic acid, and (*S*)-mandelic acid. The VCD intensities of the cocrystal spectra are multiplied by five for better visibility. The spectra of (*R*)-ivabradine.HCl, the mixture, and cocrystals were offset from (*R*)-mandelic acid by 1.0, 1.7, 2.6, and 3.4 (IR) and by 0.0012, 0.0025, 0.0040, and 0.0050 (VCD).

of available functionals is limited. Therefore, we see the fragmentation and transfer approach offering greater flexibility as a suitable compromise between the accuracy and computational cost, as documented previously on studies including Raman, IR, or VCD spectra of similar solid-state systems [49,57,59].

3.3. Advantages and limitations of employed techniques

The examples inspected above highlight the complementarity of the techniques in the characterization of different diastereomeric cocrystals. Low-frequency Raman spectroscopy provides the fastest analyses (minutes) and is highly sensitive to differences in crystal packing through lattice vibrational modes, making it an ideal tool for the rapid screening and detection of structurally distinct phases. However, its crystal-packing sensitivity decreases significantly for nearly isostructural systems. It is also inherently insensitive to chirality, as is ssNMR.

Solid-state NMR operates on a longer timescale but offers a more localized site-specific insight into the local chemical environments and intermolecular interactions. This appeared especially convenient for ivabradine, where it discriminated structural differences in the local geometry or hydrogen bonding.

VCD is inherently sensitive to the absolute configuration and extremely sensitive also to fine structural differences; however, the high noise-to-signal ratio resulting in long measurement times limits its applications.

For all spectroscopies, a computational apparatus is developed, enabling faithful modeling based on DFT and utilizing either periodic plane-wave or cluster models. However, their extensive computational requirements may significantly limit their practical use. For example, cluster models quickly become too large for crystals consisting of large molecules, or the plane-wave methodology does not allow the efficient use of hybrid functionals needed for accurate results.

In simplified summary, Raman spectroscopy is best suited for the rapid screening and monitoring of cocrystal formation, ssNMR for structural refinement and interpretation of intermolecular interactions, and VCD, supported by quantum-chemical calculations, for definitive chiral discrimination and assignment of absolute configuration. This complementarity is summarized in Table 1 and underpins the suggested analytical workflow proposed in Fig. 9.

4. Conclusions

In this study, we evaluated the resolving power of ssNMR, IR, Raman, and VCD spectroscopy in terms of the analysis of diastereomeric drug-containing cocrystals. Two representative model systems were examined: (*S*)-naproxen/(*R*)- or (*S*)-alanine cocrystal and (*R*)-ivabradine hydrochloride/(*R*)- or (*S*)-mandelic acid cocrystal. The experimental spectra were acquired and interpreted using quantum chemical calculations.

While all techniques provided clear differences indicative of cocrystal formation, VCD showed the most pronounced discrimination. The pure enantiomers exhibited mirror-image VCD spectra, whereas the diastereomeric cocrystal pairs often differed in terms of band signs, frequencies, and shapes. VCD was the only method that detected perturbations in the carbonyl moiety induced by the co-grinding of the individual components. On the other hand, there are some practical limitations of ssVCD. The measurement time, typically several hours, combined with the need for careful preparation of the pellets to maintain optimal absorbance and minimize the noise, poses a significant obstacle to high-throughput applications. However, the inherently weak VCD signal requires careful sample preparation and extended acquisition times to obtain reliable spectra.

The ^{13}C NMR spectra provided clearly visible spectral differences for the (*S*)-naproxen/alanine cocrystals, whereas the differences for the nearly isostructural ivabradine hydrochloride/mandelic acid pairs were more subtle and less obvious. DFT calculations of the NMR spectra were in good agreement with the experiment and enabled a complete atom-specific interpretation of the experimental spectra.

Raman spectroscopy also differentiated diastereomeric cocrystals. Although this method does not distinguish between enantiomers, structurally distinct diastereomers can be resolved in a relatively short time compared to VCD (typically tens of minutes, depending on the number of points mapped). However, as shown for ivabradine cocrystals, Raman spectroscopy appeared less suitable for isostructural diastereomers.

Computational models have greatly extended our understanding and enabled detailed interpretation of experiments. Nevertheless, future improvements in computational methodologies are highly desirable, such as the incorporation of molecular dynamics, temperature, and anharmonicity effects. Computationally cheaper periodic calculations should eliminate the artifacts of cluster models.

In a simplified manner, we propose a hierarchical analytical workflow for the development and quality control of chiral cocrystals: (*i*) primary screening by LF-Raman spectroscopy, (*ii*) structural monitoring refinement by ssNMR, and (*iii*) definitive chiral identification by IR/VCD.

CRediT authorship contribution statement

Věra Schrenková: Conceptualization, Formal analysis, Investigation, Visualization, Writing – original draft. **Adam Sklenář:** Formal analysis, Investigation, Visualization, Writing – original draft. **Martin**

Table 1
A simplified overview of the four spectroscopic methods.

	ssNMR	Raman	IR	ssVCD
Speed	moderate	moderate/fast	fast	slow
Chirality sensitivity	no	no	no	yes
Distinct crystal packing sensitivity	high	high	moderate	high
"Isostructural" resolution	moderate	moderate/ poor	moderate	high
Cost / Complexity	moderate	low	low	high

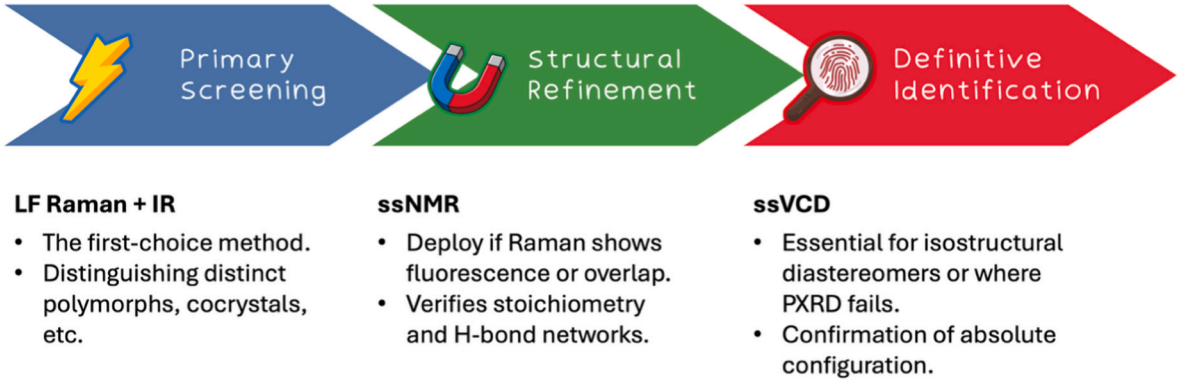


Fig. 9. Proposed analytical hierarchy for pharmaceutical applications.

Dračínský: Formal analysis, Investigation, Resources, Supervision, Writing – review & editing. **Jan Rohlíček:** Formal analysis, Investigation. **Petr Bouř:** Funding acquisition, Methodology, Supervision, Writing – review & editing. **Argyro Chatziadi:** Formal analysis, Investigation, Writing – review & editing. **Jakub Kaminský:** Conceptualization, Formal analysis, Investigation, Methodology, Project administration, Supervision, Validation, Visualization, Writing – original draft.

Declaration of competing interest

The authors declare that they have no known competing financial interests or personal relationships that could have appeared to influence the work reported in this paper.

Acknowledgments

This study was supported by the Czech Science Foundation (Petr Bouř; 24-10558S) and Ministry of Education, Youth and Sports of the Czech Republic through the Inter-COST program (Martin Dračínský; LUC24101). Computational resources were provided by the e-INFRA CZ project (ID:90254), supported by the Ministry of Education, Youth and Sports of the Czech Republic.

Appendix A. Supplementary data

Supplementary data to this article can be found online at https://doi.org/10.1016/j.talanta.2026.130238.

Data availability

Data are available at: https://osf.io/nx4ej/

Resolution Of Chiral Drug Cocrystals: Complementary Roles Of NMR, Terahertz Raman And Vibrational Circular Dichroism (Original data) (OSF.)

References

[1] N.K. Duggirala, M.L. Perry, Ö. Almarsson, M.J. Zaworotko, Pharmaceutical cocrystals: along the path to improved medicines, Chem. Commun. 52 (2016) 640–655, https://doi.org/10.1039/C5CC08216A.
[2] A.V. Yadav, A.S. Shete, A.P. Dabke, P.V. Kulkarni, S.S. Sakhare, Co-crystals: a novel approach to modify physicochemical properties of active pharmaceutical ingredients, Indian J. Pharmaceut. Sci. 71 (2009) 359–370, https://doi.org/10.4103/0250-474X.57283.
[3] H. He, Y. Huang, Q. Zhang, J.-R. Wang, X. Mei, Zwitterionic cocrystals of flavonoids and proline: solid-state characterization, pharmaceutical properties, and pharmacokinetic performance, Cryst. Growth Des. 16 (2016) 2348–2356, https://doi.org/10.1021/acs.cgd.6b00142.
[4] P. Sanphui, V.K. Devi, D. Clara, N. Malviya, S. Ganguly, G.R. Desiraju, Cocrystals of hydrochlorothiazide: solubility and diffusion/permeability enhancements through drug–coformer interactions, Mol. Pharm. 12 (2015) 1615–1622, https://doi.org/10.1021/acs.molpharmaceut.5b00020.
[5] M.L. Cheney, D.R. Weyna, N. Shan, M. Hanna, L. Wojtas, M.J. Zaworotko, Coformer selection in pharmaceutical cocrystal development: a case study of a meloxicam aspirin cocrystal that exhibits enhanced solubility and pharmacokinetics, J. Pharm. Sci. 100 (2011) 2172–2181, https://doi.org/10.1002/jps.22434.
[6] A. Chettri, A. Subba, G.P. Singh, P.P. Bag, Pharmaceutical co-crystals: a green way to enhance drug stability and solubility for improved therapeutic efficacy, J. Pharm. Pharmacol. 76 (2024) 1–12, https://doi.org/10.1093/jpp/rgad097.
[7] S.S. Buddhadev, K.C. Garala, Pharmaceutical cocrystals—A review, Proceedings 62 (2020) 14, https://doi.org/10.3390/proceedings2020062014.
[8] C. Dhakate, Taste masking by co-crystallization: a review, World J. Pharmaceut. Res. (2017) 1531–1548, https://doi.org/10.20959/wjpr20177-8881.
[9] V. Sládková, O. Dammer, G. Sedmak, E. Skořepová, B. Kratochvíl, Ivabradine hydrochloride (S)-Mandelic acid co-crystal: in situ preparation during formulation, Crystals 7 (2017) 13, https://doi.org/10.3390/cryst7010013.
[10] M. Inoue, H. Hisada, T. Koide, J. Carriere, R. Heyler, T. Fukami, Real-time formation monitoring of cocrystals with different stoichiometries using probe-type low-frequency raman spectroscopy, Ind. Eng. Chem. Res. 56 (44) (2017) 12693–12697, https://doi.org/10.1021/acs.iecr.7b03141.
[11] G. Bolla, A. Nangia, Pharmaceutical cocrystals: walking the talk, Chem. Commun. 52 (2016) 8342–8360, https://doi.org/10.1039/C6CC02943D.
[12] U.S.F.a.D. Administration, in: C.f.D.E.a. Research (Ed.), Regulatory Classification of Pharmaceutical Co-Crystals Guidance for Industry, 2018.
[13] N. Abbas, S. Latif, H. Afzal, M.S. Arshad, A. Hussain, S. Sadeeqa, N.I. Bukhari, Simultaneously improving mechanical, formulation, and in vivo performance of naproxen by Co-Crystallization, AAPS PharmSciTech 19 (2018) 3249–3257, https://doi.org/10.1208/s12249-018-1152-7.
[14] M. Yaghoobi, T. Grecu, S. Brookes, C.J. Campbell, Automatic cocrystal detection by raman spectral deconvolution-based novelty analysis, Anal. Chem. 93 (2021) 14375–14382, https://doi.org/10.1021/acs.analchem.1c01082.
[15] N. Suzuki, K. Fukui, K. Otaka, T. Suzuki, T. Fukami, Monitoring of cocrystal dissociation during the wet granulation process in the presence of disintegrants by using low-frequency raman spectroscopy, Chem. Pharm. Bull. 69 (2021) 877–885, https://doi.org/10.1248/cpb.c21-00302.
[16] B.S. Sekhon, Drug-drug co-crystals, Daru J. Pharm. Sci. 20 (2012) 45, https://doi.org/10.1016/j.ajps.2020.06.004.
[17] R. Thipparaboina, D. Kumar, R.B. Chavan, N.R. Shastri, Multidrug co-crystals: towards the development of effective therapeutic hybrids, Drug Discov. Today 21 (2016) 481–490, https://doi.org/10.1016/j.drudis.2016.02.001.
[18] F.H. Roche, Swiss Patent CH 187826:1937, Basel (Switzerland), 1937.
[19] M. Guo, X. Sun, J. Chen, T. Cai, Pharmaceutical cocrystals: a review of preparations, physicochemical properties and applications, Acta Pharm. Sin. B 11 (2021) 2537–2564, https://doi.org/10.1016/j.apsb.2021.03.030.
[20] P. Li, Y. Chu, L. Wang, R.M. Wenslow, K. Yu, H. Zhang, Z. Deng, Structure determination of the theophylline–nicotinamide cocrystal: a combined powder XRD, 1D solid-state NMR, and theoretical calculation study, CrystEngComm 16 (2014) 3141–3147, https://doi.org/10.1039/C4CE00012A.
[21] H. Yamashita, Y. Hirakura, M. Yuda, K. Terada, Coformer screening using thermal analysis based on binary phase diagrams, Pharm. Res. 31 (2014) 1946–1957, https://doi.org/10.1007/s11095-014-1296-4.
[22] E. Pindelska, A. Sokal, W. Kolodziejski, Pharmaceutical cocrystals, salts and polymorphs: advanced characterization techniques, Adv. Drug Deliv. Rev. 117 (2017) 111–146, https://doi.org/10.1016/j.addr.2017.09.014.
[23] A.A. Bunaciu, E.G. Udriştioiu, H.Y. Aboul-Enein, X-Ray diffraction: instrumentation and applications, Crit. Rev. Anal. Chem. 45 (2015) 289–299, https://doi.org/10.1080/10408347.2014.949616.
[24] J.M. Kim, S. Lim, M. Kim, E. Ban, Y. Kim, A. Kim, Using the cocrystal approach as a promising drug delivery system to enhance the dissolution and bioavailability of formononetin using an imidazole coformer, Pharmaceuticals 17 (2024) 1444, https://doi.org/10.3390/ph17111444.
[25] T.G. Fawcett, S. Gates-Rector, A.M. Gindhart, M. Rost, S.N. Kabekkodu, J. R. Blanton, T.N. Blanton, A practical guide to pharmaceutical analyses using X-ray

powder diffraction, Powder Diffr. 34 (2019) 164–183, https://doi.org/10.1017/S088571561900023X.
[26] T.N. Pham, S.A. Watson, A.J. Edwards, M. Chavda, J.S. Clawson, M. Strohmeier, F. G. Vogt, Analysis of amorphous solid dispersions using 2D solid-state NMR and 1H T1 relaxation measurements, Mol. Pharm. 7 (2010) 1667–1691, https://doi.org/10.1021/mp100205g.
[27] A. Pugliese, M. Toresco, D. McNamara, D. Iuga, A. Abraham, M. Tobyn, L. E. Hawarden, F. Blanc, Drug–polymer interactions in acetaminophen/hydroxypropylmethylcellulose acetyl succinate amorphous solid dispersions revealed by multidimensional multinuclear solid-state NMR spectroscopy, Mol. Pharm. 18 (2021) 3519–3531, https://doi.org/10.1021/acs.molpharmaceut.1c00427.
[28] F.G. Vogt, J.S. Clawson, M. Strohmeier, A.J. Edwards, T.N. Pham, S.A. Watson, Solid-state NMR analysis of organic cocrystals and complexes, Cryst. Growth Des. 9 (2) (2009) 921–937, https://doi.org/10.1021/cg8007014.
[29] M. Zilka, J.R. Yates, S.P. Brown, An NMR crystallography investigation of furosemide, Magn. Reson. Chem. 57 (2019) 191–199, https://doi.org/10.1002/mrc.4789.
[30] L. Rajput, M. Banik, J.R. Yarava, S. Joseph, M.K. Pandey, Y. Nishiyama, G. R. Desiraju, Exploring the salt-cocrystal continuum with solid-state NMR using natural-abundance samples: implications for crystal engineering, IUCrJ 4 (2017) 466–475, https://doi.org/10.1107/s205225251700687x.
[31] L. Zhao, M.P. Hanrahan, P. Chakravarty, A.G. DiPasquale, L.E. Sirois, K. Nagapudi, J.W. Lubach, A.J. Rossini, Characterization of pharmaceutical cocrystals and salts by dynamic nuclear polarization-enhanced solid-state NMR spectroscopy, Cryst. Growth Des. 18 (2018) 2588–2601, https://doi.org/10.1021/acs.cgd.8b00203.
[32] J. Blahut, J.R. Štoček, M. Šála, M. Dračínský, The hydrogen bond continuum in solid isonicotinic acid, J. Magn. Reson. 345 (2022) 107334, https://doi.org/10.1016/j.jmr.2022.107334.
[33] M. Dračínský, NMR spectroscopy studies of hydrogen bonding, Coord. Chem. Rev. 549 (2025) 217284, https://doi.org/10.1016/j.ccr.2025.217284.
[34] J.R. Štoček, J. Blahut, S. Chalupná, J. Čejka, S. Štěpánová, V. Kašička, M. Hušák, M. Dračínský, The hydrogen-bond continuum in the salt/cocrystal systems of quinoline and chloro-nitrobenzoic acids, Chem. Eur J. 30 (2024) e202402946, https://doi.org/10.1002/chem.202402946.
[35] J.R. Štoček, O. Socha, I. Císařová, T. Slanina, M. Dračínský, Importance of nuclear quantum effects for molecular cocrystals with short hydrogen bonds, J. Am. Chem. Soc. 144 (2022) 7111–7116, https://doi.org/10.1021/jacs.1c10885.
[36] Q. Jiang, R.K. Ghosh, G.A. Valdivia-Berroeta, B.J. Walder, L. Luo, Deciphering imatinib multicomponent crystals: insights from X-Ray crystallography and solid-state NMR spectroscopy, Cryst. Growth Des. 25 (2025) 1978–1991, https://doi.org/10.1021/acs.cgd.4c01419.
[37] K. Maruyoshi, D. Iuga, A.E. Watts, C.E. Hughes, K.D.M. Harris, S.P. Brown, Assessing the detection limit of a minority solid-state form of a pharmaceutical by 1H double-quantum magic-angle spinning nuclear magnetic resonance spectroscopy, J. Pharm. Sci. 106 (2017) 3372–3377, https://doi.org/10.1016/j.xphs.2017.07.014.
[38] Y.-L. Hong, G.N. Manjunatha Reddy, Y. Nishiyama, Selective detection of active pharmaceutical ingredients in tablet formulations using solid-state NMR spectroscopy, Solid State Nucl. Magn. Reson. 106 (2020) 101651, https://doi.org/10.1016/j.ssnmr.2020.101651.
[39] M. Dračínský, E. Procházková, J. Kessler, J. Šebestík, P. Matějka, P. Bouř, Resolution of organic polymorphic crystals by Raman spectroscopy, J. Phys. Chem. B 117 (2013) 7297–7307, https://doi.org/10.1021/jp404382f.
[40] M.F. Khairi, S. Abdullah, M.A.A.-T. Moawia, A.A. Akram, Recent applications of quantitative analytical FTIR spectroscopy in pharmaceutical, biomedical, and clinical fields: a brief review, Rev. Anal. Chem. 41 (2022) 21–33, https://doi.org/10.1515/revac-2022-0030.
[41] N. Eshbekova, A. Sowndarya, T.D. Thangadurai, Y.-I. Lee, Recent advancements in Raman instrumentation and capabilities for pharmaceutical and biomedical applications, Appl. Spectrosc. Rev. 59 (2024) 798–849, https://doi.org/10.1080/05704928.2024.2355193.
[42] L. Shi, N. Wang, X. Huang, T. Wang, H. Hao, L. Zhou, Chiral resolution of dl-Leucine by the diastereomeric salt/cocrystal method, Cryst. Growth Des. 25 (2025) 8450–8460, https://doi.org/10.1021/acs.cgd.5c00809.
[43] J. Carriere, F. Havermeyer, Ultra-low frequency Stokes and anti-Stokes Raman spectroscopy at 785nm with volume holographic grating filters, Progr. Biomed. Opt. Imaging 8219 (2012) 3, https://doi.org/10.1117/12.909463.
[44] J. Kim, J.-U. Lee, H. Cheong, Polarized Raman spectroscopy for studying two-dimensional materials, J. Phys. Condens. Matter 32 (2020) 343001, https://doi.org/10.1088/1361-648X/ab8848.
[45] P.J. Larkin, J. Wasylyk, M. Raglione, Application of Low- and mid-frequency raman spectroscopy to characterize the amorphous-crystalline transformation of indomethacin, Appl. Spectrosc. 69 (2015) 1217–1228, https://doi.org/10.1366/15-07926.
[46] J. Koskela, J.J. Sutton, T. Lipiäinen, K.C. Gordon, C.J. Strachan, S.J. Fraser-Miller, Low- versus mid-frequency raman spectroscopy for in situ analysis of crystallization in slurries, Mol. Pharm. 19 (2022) 2316–2326, https://doi.org/10.1021/acs.molpharmaceut.2c00126.
[47] S. Hubert, S. Briancon, A. Hedoux, Y. Guinet, L. Paccou, H. Fessi, F. Puel, Process induced transformations during tablet manufacturing: phase transition analysis of caffeine using DSC and low frequency micro-Raman spectroscopy, Int. J. Pharm. 420 (2011) 76–83, https://doi.org/10.1016/j.ijpharm.2011.08.028.
[48] A.P. Ayala, Polymorphism in drugs investigated by low wavenumber Raman scattering, Vib. Spectrosc. 45 (2007) 112–116, https://doi.org/10.1016/j.vibspec.2007.06.004.
[49] V. Schrenková, J. Kapitán, P. Bouř, A. Chatziadi, A. Sklenář, J. Kaminský, Sofosbuvir polymorphs distinguished by linearly and circularly polarized raman microscopy, Anal. Chem. 96 (2024) 18983–18993, https://doi.org/10.1021/acs.analchem.4c03573.
[50] K. Bērziņš, R.E. Sales, J.E. Barnsley, G. Walker, S.J. Fraser-Miller, K.C. Gordon, Low-wavenumber Raman spectral database of pharmaceutical excipients, Vib. Spectrosc. 107 (2020) 103021, https://doi.org/10.1016/j.vibspec.2020.103021.
[51] L.A. Papp, S. Krizbai, M. Dobó, G. Hancu, Z.I. Szabó, G. Tóth, Determination of chiral impurity of naproxen in different pharmaceutical formulations using polysaccharide-based stationary phases in reversed-phased mode, Molecules 27 (2022), https://doi.org/10.3390/molecules27092986.
[52] M. Inoue, T. Osada, H. Hisada, T. Koide, T. Fukami, A. Roy, J. Carriere, R. Heyler, Solid-state quantification of cocrystals in pharmaceutical tablets using transmission low-frequency raman spectroscopy, Anal. Chem. 91 (2019) 13427–13432, https://doi.org/10.1021/acs.analchem.9b01895.
[53] Z. Pei, C. Ji, M. Shao, Y. Wu, X. Zhao, B. Man, Z. Li, J. Yu, C. Zhang, Enrichment strategies in surface-enhanced Raman scattering: theoretical insights and optical design for enhanced light-matter interaction, opto-electron, Sci. 4 (2025) 250015, https://doi.org/10.29026/oes.2025.250015.
[54] T. Firkala, A. Farkas, B. Vajna, Z.K. Nagy, G. Pokol, G. Marosi, I.M. Szilágyi, Quantification of low drug concentration in model formulations with multivariate analysis using surface enhanced Raman chemical imaging, J. Pharm. Biomed. Anal. 107 (2015) 318–324, https://doi.org/10.1016/j.jpba.2014.12.039.
[55] H. Sato, I. Kawamura, Solid-state vibrational circular dichroism studies on the conformation of an amino acid molecule in crystalline state, Biochim. Biophys. Acta Proteins Proteom 1868 (2020) 140439, https://doi.org/10.1016/j.bbapap.2020.140439.
[56] K. Dobšíková, T. Taušová, P. Fagan, N. Paškanová, M. Kuchař, J. Čejka, V. Setnička, Solid-state vibrational circular dichroism: methodology and application for amphetamine derivatives, Spectrochim. Acta Mol. Biomol. Spectrosc. 305 (2024) 123486, https://doi.org/10.1016/j.saa.2023.123486.
[57] A. Sklenář, L. Růžičková, V. Schrenková, L. Bednárová, M. Pazderková, A. Chatziadi, E. Zmeškalová Skořepová, M. Šoóš, J. Kaminský, Solid-state vibrational circular dichroism for pharmaceutical applications: polymorphs and cocrystal of sofosbuvir, Spectrochim. Acta Mol. Biomol. Spectrosc. 318 (2024) 124478, https://doi.org/10.1016/j.saa.2024.124478.
[58] J. Frelek, M. Górecki, M. Łaszcz, A. Suszczyńska, E. Vass, W.J. Szczepek, Distinguishing between polymorphic forms of linezolid by solid-phase electronic and vibrational circular dichroism, Chem. Commun. 48 (2012) 5295–5297, https://doi.org/10.1039/C2CC31207G.
[59] A. Sklenář, A. Zehnacker-Rentien, J. Kaminský, J. Rohlíček, P. Bouř, Exploring naproxen cocrystals through solid-state vibrational circular dichroism, Chirality 37 (2025) e70027, https://doi.org/10.1002/chir.70027.
[60] M. Krupová, P. Leszczenko, E. Sierka, S.E. Hamplová, R. Pelc, V. Andrushchenko, Vibrational circular dichroism unravels supramolecular chirality and hydration polymorphism of nucleoside crystals, Chem. Eur J. 28 (2022) e202201922, https://doi.org/10.1002/chem.202201922.
[61] J.E. Rode, J. Wasilczenko, M. Górecki, Differentiation of solvatomorphs of active pharmaceutical ingredients (API) by solid-state vibrational circular dichroism (VCD), Spectrochim. Acta Mol. Biomol. Spectrosc. 310 (2024) 123851, https://doi.org/10.1016/j.saa.2024.123851.
[62] R. Kaviani, A. Jouyban, A. Shayanfar, Chiral resolution methods for racemic pharmaceuticals based on cocrystal formation, CrystEngComm 25 (2023) 6120–6131, https://doi.org/10.1039/D3CE00853C.
[63] G. Springuel, T. Leyssens, Innovative chiral resolution using enantiospecific Co-Crystallization in solution, Cryst. Growth Des. 12 (2012) 3374–3378, https://doi.org/10.1021/cg300307z.
[64] S. Iwama, K. Kuyama, Y. Mori, K. Manoj, R.G. Gonnade, K. Suzuki, C.E. Hughes, P. A. Williams, K.D.M. Harris, S. Veesler, H. Takahashi, H. Tsue, R. Tamura, Highly efficient chiral resolution of dl-Arginine by cocrystal formation followed by recrystallization under preferential-enrichment conditions, Chem. Eur J. 20 (2014) 10343–10350, https://doi.org/10.1002/chem.201402446.
[65] H. Wu, A.R. West, M. Vickers, D.C. Apperley, A.G. Jones, Synthesis, crystallization and characterization of diastereomeric salts formed by ephedrine and malic acid in water, Chem. Eng. Sci. 77 (2012) 47–56, https://doi.org/10.1016/j.ces.2011.12.007.
[66] G. Springuel, K. Robeyns, B. Norberg, J. Wouters, T. Leyssens, Cocrystal formation between chiral compounds: how cocrystals differ from salts, Cryst. Growth Des. 14 (2014) 3996–4004, https://doi.org/10.1021/cg500588t.
[67] M. Habgood, Analysis of enantiospecific and diastereomeric cocrystal systems by crystal structure prediction, Cryst. Growth Des. 13 (2013) 4549–4558, https://doi.org/10.1021/cg401040p.
[68] S. Songsermsawad, K. Boonpalit, O. Shemchuk, K. Robeyns, T. Leyssens, A. E. Flood, Stereochemical control of cocrystal and hybrid salt−cocrystal formation in the baclofen−mandelic acid system, Cryst. Growth Des. 25 (2025) 6830–6836, https://doi.org/10.1021/acs.cgd.5c00779.
[69] H.D.W. Hill, A.P. Zens, J. Jacobus, Solid-state NMR spectroscopy. Distinction of diastereomers and determination of optical purity, J. Am. Chem. Soc. 101 (1979) 7090–7091, https://doi.org/10.1021/ja00517a063.
[70] J.M. Kim, S.M. Chang, I.H. Kim, X.H. Pham, W.S. Kim, Investigating chiral recognizability of diastereomeric crystallization of mandelic acid and L-Phenylalanine, J. Nanosci. Nanotechnol. 12 (2012) 7139–7147, https://doi.org/10.1166/jnn.2012.6490.
[71] N. Suzuki, T. Kawasaki, Evaluation of solid state form of troglitazone by solid state NMR spectroscopy, J. Pharm. Biomed. Anal. 37 (2005) 177–181, https://doi.org/10.1016/j.jpba.2004.09.035.

[72] S.W. Wong, C. Georgakis, G.D. Botsaris, K. Saranteas, R. Bakale, Online estimation of diastereomer composition using raman: differentiation in high and low slurry density partial least square models, Cryst. Growth Des. 8 (2008) 4398–4408, https://doi.org/10.1021/cg701201x.
[73] C.S. Wallace, M.P. Davis, T.M. Korter, Low-frequency raman spectroscopy of pure and cocrystallized mycophenolic acid, Pharmaceutics 15 (2023) 1924, https://doi.org/10.3390/pharmaceutics15071924.
[74] M.P. Davis, T.M. Korter, Evaluating hydrogen bonding in organic cocrystals using low-frequency raman vibrational spectroscopy and quantum mechanical simulations, Cryst. Growth Des. 22 (2022) 1922–1932, https://doi.org/10.1021/acs.cgd.1c01474.
[75] P. Ma, B. Toussaint, E.A. Roberti, N. Scornet, A. Santos Silva, L. Castillo Henríquez, M. Cadasse, P. Négrier, S. Massip, H. Dufat, K. Hammad, C. Baraldi, M. C. Gamberini, C. Richard, S. Veesler, P. Espeau, T. Lee, Y. Corvis, New lidocaine-based pharmaceutical cocrystals: preparation, characterization, and influence of the racemic vs. enantiopure coformer on the physico-chemical properties, Pharmaceutics 15 (2023) 1102, https://doi.org/10.3390/pharmaceutics15041102.
[76] N. Tumanova, N. Tumanov, K. Robeyns, Y. Filinchuk, J. Wouters, T. Leyssens, Structural insight into cocrystallization with zwitterionic co-formers: cocrystals of S-naproxen, CrystEngComm 16 (2014) 8185–8196, https://doi.org/10.1039/C4CE00353E.
[77] C. Xing, T. Chen, L. Wang, Q. An, Y. Jin, D. Yang, L. Zhang, G. Du, Y. Lu, Two novel Co-Crystals of naproxen: comparison of stability, solubility and intermolecular interaction, Pharmaceuticals 15 (2022) 807, https://doi.org/10.3390/ph15070807.
[78] Y. Kamisah, H.H. Che Hassan, Therapeutic use and molecular aspects of ivabradine in cardiac remodeling: a review, Int. J. Mol. Sci. 24 (2023) 2801, https://doi.org/10.3390/ijms24032801.
[79] S. Latif, Q.A. Ijaz, M. Hameed, Q. Shoaib, K. Fatima, A. Hussain, M.S. Arshad, N. Abbas, Improvement of Physico-mechanical and pharmacokinetic attributes of naproxen by cocrystallization with l-alanine, J. Drug Deliv. Technol. 61 (2021) 102236, https://doi.org/10.1016/j.jddst.2020.102236.
[80] P. Bouř, Program sc95, Institute of Organic Chemistry and Biochemistry of the CAS, 2024. Prague, Czech Republic.
[81] S.J. Clark, M.D. Segall, C.J. Pickard, P.J. Hasnip, M.J. Probert, K. Refson, M. C. Payne, First principles methods using CASTEP, Z. Kristallogr. 220 (2005) 567–570, https://doi.org/10.1524/zkri.220.5.567.65075.
[82] J.P. Perdew, K. Burke, M. Ernzerhof, Generalized gradient approximation made simple, Phys. Rev. Lett. 77 (1996) 3865–3868, https://doi.org/10.1103/PhysRevLett.77.3865.
[83] D. Vanderbilt, Soft self-consistent pseudopotentials in a generalized eigenvalue formalism, Phys. Rev. B 41 (1990) 7892–7895, https://doi.org/10.1103/PhysRevB.41.7892.
[84] H.J. Monkhorst, J.D. Pack, Special points for brillouin-zone integrations, Phys. Rev. B 13 (1976) 5188–5192, https://doi.org/10.1103/PhysRevB.13.5188.
[85] A. Tkatchenko, M. Scheffler, Accurate Molecular Van Der Waals Interactions from Ground-State Electron Density and Free-Atom Reference Data, Phys. Rev. Lett. 102 (2009) 073005, https://doi.org/10.1103/PhysRevLett.102.073005.
[86] C.J. Pickard, F. Mauri, All-electron magnetic response with pseudopotentials: NMR chemical shifts, Phys. Rev. B 6324 (2001) 245101, https://doi.org/10.1103/PhysRevB.63.245101.
[87] J.R. Yates, C.J. Pickard, F. Mauri, Calculation of NMR chemical shifts for extended systems using ultrasoft pseudopotentials, Phys. Rev. B 76 (2007) 024401, https://doi.org/10.1103/PhysRevB.76.024401.
[88] F.H. Allen, The Cambridge structural database: a quarter of a million crystal structures and rising, Acta Crystallogr. B58 (2002) 380–388, https://doi.org/10.1107/s0108768102003890.
[89] C.F. Macrae, I. Sovago, S.J. Cottrell, P.T.A. Galek, P. McCabe, E. Pidcock, M. Platings, G.P. Shields, J.S. Stevens, M. Towler, P.A. Wood, Mercury 4.0: from visualization to analysis, design and prediction, J. Appl. Crystallogr. 53 (2020) 226–235, https://doi.org/10.1107/s1600576719014092.
[90] S. Grimme, Semiempirical GGA-type density functional constructed with a long-range dispersion correction, J. Comput. Chem. 27 (2006) 1787–1799, https://doi.org/10.1002/jcc.20495.
[91] P. Bouř, T.A. Keiderling, Partial optimization of molecular geometry in normal coordinates and use as a tool for simulation of vibrational spectra, J. Chem. Phys. 117 (2002) 4126–4132, https://doi.org/10.1063/1.1498468.
[92] P. Bouř, Program QGRAD, Institute of Organic Chemistry and Biochemistry of the CAS, 2020. Prague, Czech Republic.
[93] M.J. Frisch, G.W. Trucks, H.B. Schlegel, G.E. Scuseria, M.A. Robb, J.R. Cheeseman, G. Scalmani, V. Barone, G.A. Petersson, H. Nakatsuji, X. Li, M. Caricato, A. V. Marenich, J. Bloino, B.G. Janesko, R. Gomperts, B. Mennucci, H.P. Hratchian, J. V. Ortiz, A.F. Izmaylov, J.L. Sonnenberg, Williams, F. Ding, F. Lipparini, F. Egidi, J. Goings, B. Peng, A. Petrone, T. Henderson, D. Ranasinghe, V.G. Zakrzewski, J. Gao, N. Rega, G. Zheng, W. Liang, M. Hada, M. Ehara, K. Toyota, R. Fukuda, J. Hasegawa, M. Ishida, T. Nakajima, Y. Honda, O. Kitao, H. Nakai, T. Vreven, K. Throssell, J.A. Montgomery Jr., J.E. Peralta, F. Ogliaro, M.J. Bearpark, J. J. Heyd, E.N. Brothers, K.N. Kudin, V.N. Staroverov, T.A. Keith, R. Kobayashi, J. Normand, K. Raghavachari, A.P. Rendell, J.C. Burant, S.S. Iyengar, J. Tomasi, M. Cossi, J.M. Millam, M. Klene, C. Adamo, R. Cammi, J.W. Ochterski, R.L. Martin, K. Morokuma, O. Farkas, J.B. Foresman, D.J. Fox, Gaussian 16, Rev. C.01, Wallingford, CT, 2016.
[94] Y. Takano, K.N. Houk, Benchmarking the Conductor-like polarizable continuum model (CPCM) for aqueous solvation free energies of neutral and ionic organic molecules, J. Chem. Theor. Comput. 1 (2005) 70–77, https://doi.org/10.1021/ct049977a.
[95] P. Bouř, J. Sopková, L. Bednárová, P. Maloň, T.A. Keiderling, Transfer of molecular property tensors in Cartesian coordinates: a new algorithm for simulation of vibrational spectra, J. Comput. Chem. 18 (1997) 646–659, https://doi.org/10.1002/(SICI)1096-987X(19970415)18:5<646::AID-JCC6>3.0.CO;2-N.
[96] M. Dračínský, P. Hodgkinson, Effects of quantum nuclear delocalisation on NMR parameters from path integral molecular dynamics, Chem. Eur J. 20 (2014) 2201–2207, https://doi.org/10.1002/chem.201303496.
[97] S. Jähnigen, K. LeBarbu-Debus, R. Guillot, R. Vuilleumier, A. Zehnacker, How crystal symmetry dictates non-local vibrational circular dichroism in the solid state, Angew. Chem. Int. Ed. 62 (2023) e202215599, https://doi.org/10.1002/anie.202215599.
[98] S. Jähnigen, A. Scherrer, R. Vuilleumier, D. Sebastiani, Chiral crystal packing induces enhancement of vibrational circular dichroism, Angew. Chem. Int. Ed. 57 (2018) 13344–13348, https://doi.org/10.1002/anie.201805671.